Position-sensitive detectors based on redshifts in photoluminescence spectra

Yasuhiro Tsutsumi
Ryo Matsumura
Masamichi Ohta
Ichiro Fujieda

Position-sensitive detectors based on redshifts in photoluminescence spectra

Yasuhiro Tsutsumi,* Ryo Matsumura, Masamichi Ohta, and Ichiro Fujieda
Ritsumeikan University, Department of Electrical and Electronic Engineering, Kusatsu, Shiga, Japan

Abstract. We have proposed and demonstrated position-sensitive detectors based on the spectral changes in fluorescent waveguides. The first prototype is a transparent heat-shrink tubing containing an organic luminescent dye at its core. With a laser beam incident on this linear fluorescent tubing, the redshift in the photoluminescence (PL) spectrum observed at its edge increases with the distance from the incident point. The range for position sensing is 2 cm. It is extended to 280 cm by adopting a scintillating fiber in our second experiment. Two-stage conversion enables two-dimensional position detection. We have attached two linear fluorescent tubing to a planar 50 mm × 50 mm × 8 mm fluorescent waveguide. When a laser beam excites the first luminescent material at a single spot in the planer waveguide, PL photons propagate to its edges and excite the second luminescent material in the two linear waveguides. Photon division between these linear waveguides gives the first coordinate. The second coordinate is given by the redshift in the linear waveguides. We have observed that the maximum error in position estimation is 1.5 mm. Unlike the conventional semiconductor technologies, no electronic components are required for the sensor head. This robust technology might be suited for deployment in large-scale harsh environments. © *The Authors. Published by SPIE under a Creative Commons Attribution 4.0 Unported License. Distribution or reproduction of this work in whole or in part requires full attribution of the original publication, including its DOI.* [DOI: 10.1117/1 .OE.58.7.077108]

Keywords: photoluminescence; sensors; absorption; radiation.

Paper 190429 received Mar. 28, 2019; accepted for publication Jul. 10, 2019; published online Jul. 27, 2019.

1 Introduction

A position-sensitive detector (PSD) has been utilized in various applications. For example, a beam of light irradiates an object on a belt in an assembly line and a PSD detects the reflected light and generates feedback signals for automatic control. Once we get its position, we have fine control over it. In an atomic force microscope, a cantilever hanging over a specimen reflects a laser beam and a PSD detects the reflected beam. Geometrical calculation gives the displacement of the cantilever, which is a measure of the surface morphology of the nearby specimen. In high-energy physics experiments, a PSD tracks a beam of particles or electromagnetic radiation. In many PSDs, a semiconductor material converts the incoming radiation to electric charges and the charge division between multiple electrodes gives the position of the incident spot.[1–3] Even when multiple light beams hit different spots on a PSD simultaneously, one can detect their positions by modulating the light sources.[4] In general, a semiconductor device is small and expensive.[5] One-dimensional (1-D) PSDs are commercially available only up to a length of 37 mm.[6] In laboratory experiment, a PSD with a sensitive length of 74 mm is reported.[6] Although an organic/inorganic hybrid sensor structure might have the advantage of low temperature and simple fabrication process,[7] for a large-scale implementation, the use of a semiconductor substrate would be prohibitively expensive.

Historically, different approaches have been taken for realizing a large-area PSD, which happen to involve radiation detection. For example, a gamma camera has been used for many years in nuclear medicine: multiple photomultiplier tubes detect the light generated by a large slab of scintillator, and centroid calculation of their output signals gives the incident positions of the gamma rays. In this case, the photon division inside the scintillator is the operating principle.[1] For x-ray imaging, this principle does not work because so many x-ray photons are incident on a detector in a short time interval. In such a case, a pixelated detector can provide a solution. An imager based on the amorphous silicon technology has cost and size advantages, because it is a flat-panel device fabricated on a glass substrate.[8] For nonimaging, large-scale implementation of a PSD, the optical fiber sensor technology[9] has some advantages. Because its sensing part has no electric components, it is suited for usage in harsh environments as well as for insertion in narrow places. A scintillating fiber has been developed for monitoring radiation dose in a linear region. They have been tested with gamma rays[10] and in a high-energy physics experiment facility.[11] It contains a plastic scintillator in its core. It is interesting to note that a similar fiber structure with luminescent materials has been applied for converting sunlight to electricity by attaching solar cells to the end of its structure.[12] Time of flight (TOF) is its position-sensing principle: the time difference between the scintillation photons reaching the two ends of the fiber is converted to a voltage, which is related to the position of the incident radiation. Readout electronics are required at both ends of the fiber. This might pose a problem in a possible radiation therapy application where a 1-D PSD is inserted into a human body to monitor a radiation dose distribution. Nevertheless, a scintillating fiber is a 1-D PSD: it can only detect radiations incident on the fiber body. Obviously, two-dimensional (2-D) sensing is desired for monitoring radiation dose in restricted areas and contaminated regions.

*Address all correspondence to Yasuhiro Tsutsumi, E-mail: tutumi@fc.ritsumei .ac.jp

In this paper, we describe 1-D PSDs based on redshift in the photoluminescence (PL) spectrum in Sec. 2. Unlike the TOF method, there is no need to read out the signals from both ends. In Sec. 3, this concept is extended to a 2-D PSD by adopting the photon-division technique. We exploit lasers in our experiments to demonstrate this position-sensing principle in the visible range.

2 One-Dimensional Position Sensing

2.1 Basic Concept and Its Proof

In this section, we describe the operation principle and the proof-of-concept experiment reported previously.[13] In a luminescent solar concentrator (LSC),[14,15] a luminescent material embedded in a transparent plate converts sunlight to PL photons and they are harvested by the solar cells attached to the edge surfaces of the plate. Some of them are lost during the waveguiding process due to absorption by the luminescent material. This problem of self-absorption has been recognized since the early days.[16] Because it limits the power conversion efficiency of an LSC, its large-scale deployment remains unpractical. Self-absorption manifests in other negative manners. For a uniform luminescent layer where scattering events can be neglected, it causes an emission spectrum to vary with the emission angle.[17] It complicates the measurement of quantum yield of luminescent materials.

We proposed to utilize this unwanted effect for 1-D position sensing. As illustrated in Fig. 1(a), an optical fiber is coupled to the edge surface of a waveguide in which a luminescent material is uniformly dispersed. We call such a waveguide "fluorescent waveguide (FWG)" in this paper. For the moment, we work with a planar waveguide for simplicity of the experiment described below although a linear waveguide would suffice for 1-D position sensing. When an excitation beam of light is incident at $y = L$, PL photons are emitted. Some of them propagate this distance and enter the optical fiber. A spectrometer records the spectrum of the PL photons in which shorter-wavelength photons are lost due to self-absorption. The degree of this redshift in the PL spectra depends on the distance L. Hence, we can determine the incident position of the beam by quantifying it. These procedures are analyzed in the following three steps.

First, we derive the probability of collecting the PL photons by the spectrometer. Assume isotropic emission of PL photons at $y = L$. The angle θ, as defined in Fig. 1(b), is expressed as $\theta = \tan^{-1} \frac{D}{2L}$, where D is the core diameter. Numerical aperture of the optical fiber (NA) determines the

acceptance angle θ_{max}. Denoting the refractive index of the waveguide as n, the relation $n \sin \theta_{max} = NA$ holds. We assume that the refractive index is matched at the core and the waveguide. Then, the condition for the PL photon reaching the optical fiber and propagating inside is expressed as $\theta < \theta_{max}$, i.e., $\tan^{-1} \frac{D}{2L} < \sin^{-1} \frac{NA}{n}$. This condition is rewritten as

$$L > \frac{D}{2} \sqrt{\left(\frac{n}{NA}\right)^2 - 1}. \tag{1}$$

When this condition is satisfied, all the PL photons entering the optical fiber reach the spectrometer. For isotropic emission, the probability of light collection by the spectrometer η is equal to θ/π, namely

$$\eta = \frac{1}{\pi} \tan^{-1} \frac{D}{2L}. \tag{2}$$

Note that the equation above considers the geometrical effect and it neglects any loss mechanisms during the light propagation.

Second, we express the spectrum as a function of the distance L. Let $\mu(\lambda)$ be the absorption coefficient of this waveguide at wavelength λ and $S_i(\lambda)$ be the initial spectrum before redshift. The PL photon emitted with an angle θ propagates the distance $L/\cos\theta$ to reach the optical fiber. The Lambert–Beer's law gives the following expression for the spectrum of the PL photons entering the optical fiber:

$$S(\theta, \lambda) = S_i(\lambda) \exp\left[-\mu(\lambda) \cdot \frac{L}{\cos\theta}\right]. \tag{3}$$

For example, in the case of NA = 0.22, $n = 1.5$, and $D = 0.4$ mm (the conditions for the experiment described below), if $L > 1.38$ mm, all the PL photons reaching the optical fiber can propagate inside.

In case of $D/L \ll 1$, Eqs. (2) and (3) are approximated as follows:

$$\eta = \frac{D}{2\pi L}, \tag{4}$$

$$S(\theta, \lambda) = S_i(\lambda) \exp[-\mu(\lambda)L]. \tag{5}$$

Third, we have some options about how to quantify the degree of redshift. In the following experiment, we calculate
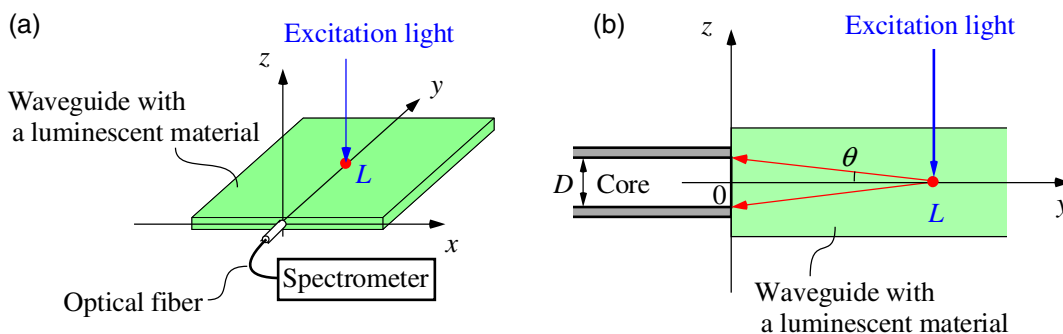

Fig. 1 One-dimensional PSD based on redshift in PL spectra. (a) A bird's eye view. (b) The cross section of the coupling section.

the chromaticity coordinates with the CIE1931 color-matching functions.

To prove this basic concept, we carried out a simple experiment using the planar FWG, which is shown in the inset of Fig. 2(a). This was supplied by Nitto Jushi Kogyo Co. Ltd. The dimension and transmittance at 450 nm of this FWG were 40 mm × 40 mm × 2.9 mm and 0.0018, respectively. The hole at the upper left corner was meant for bundling multiple samples and it did not affect our measurement. In a darkroom, we excited a single point on the FWG with a laser (Z-Laser, Model Z30M18-F-450-pe). The optics built in this laser module focused the beam, and its spot size was about 0.1 mm. The wavelength of the excitation light was 450 nm and its power was set to 83 μW. The core diameter and numerical aperture of the optical fiber (Ocean Optics, Model P400-21-VIS/NTR) were 400 μm and 0.22, respectively. The integration time of the spectrometer (Ocean Optics, Model FLMS02760) was set to 2 ms. These experimental conditions allowed us to acquire the PL spectra and they were not necessarily optimized in terms of signal-to-noise ratio. We varied the incident position of the beam along the y axis with a 2-mm step and recorded each PL spectrum. The result is shown in Fig. 2(a). As the y coordinate of the incident position (L) increases, the spectral intensity below 500 nm decreases more rapidly. This is due to self-absorption. The rate of change in the spectral intensity tends to saturate as L approaches 20 mm. In addition, we integrate each spectrum to obtain a value proportional to the PL intensity. As shown in Fig. 2(b), it is roughly proportional to the inverse of the distance L. Also shown is a fit by Eq. (4), where A is a constant. Note that the values in Fig. 2(b) are proportional to the power of the incident radiation times the integration time. Hence, once we know the incident position of radiation with unknown power, we can use Fig. 2(b) to estimate its power.

To quantify the redshift in Fig. 2(a), we used the CIE1931 color-matching functions [$\overline{x}(\lambda)$, $\overline{y}(\lambda)$, and $\overline{z}(\lambda)$] to calculate the x and y chromaticity coordinates. As shown in Fig. 3(a), the chromaticity coordinate x increases monotonically with the distance L, while the chromaticity coordinate y shows
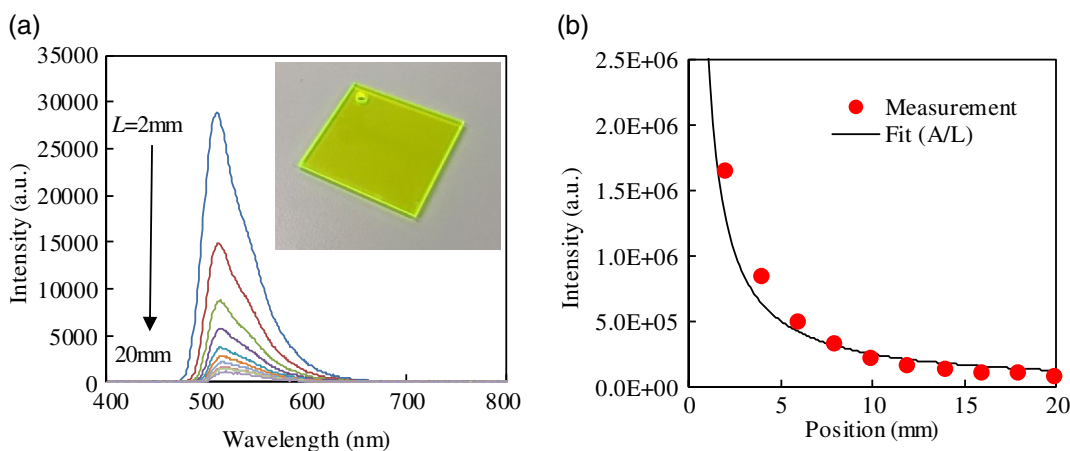

Fig. 2 PL spectrum and its integrated value corresponding to each incident point of the excitation light at 450 nm. (a) The spectral intensity below 500 nm decreases more rapidly than that above it as the distance L increases. A photograph of the planar fluorescent waveguide is shown in the inset. (b) The value obtained by integrating each spectrum in (a).
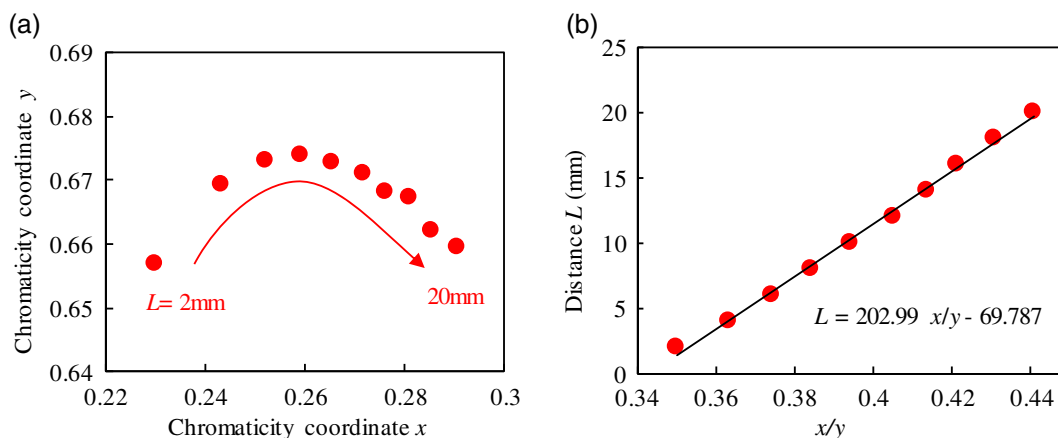

Fig. 3 Chromaticity coordinates calculated from each spectrum in Fig. 2(a). (a) The coordinates shift to a redder region as the incident position moves away from the edge surface. (b) The ratio of the chromaticity coordinates x/y is almost proportional to the distance L. The line represents a linear fitting.

a peak. In Fig. 3(b), we plot the distance L as a function of the ratio x/y. The solid circles represent the measured data and they are well fit by the following equation:

$$L = 202.99\frac{y}{x} - 69.787. \tag{6}$$

Now, we can determine the distance L from Eq. (6) by calculating the ratio x/y from the measured spectrum. Once the incident position is known, the power of the incident radiation is estimated by integrating the spectrum and comparing the result with Fig. 2(b).

2.2 Linear Fluorescent Waveguide

In the previous section, we used a planar FWG to prove the basic concept of utilizing redshift in PL spectra for 1-D position sensing. The next step was to demonstrate it with a linear FWG, which paves a way for applying this technique to a 2-D PSD. In fact, two linear FWGs were used to configure a 2-D PSD, as described in Ref. 18.

We fabricated a linear FWG by filling a hollow transparent tube with a fluorescent material. Its structure is illustrated in Fig. 4(a). In the experiment, we put a syringe needle half way into a heat-shrink tubing (Ohm Electric Inc., Tokyo, OHM 2.0C) and heated the tube by blowing hot air on it for about 10 s. We injected a mixture of a UV-curable resin (Norland, NOA81) and a luminescent material (BASF, Lumogen F Red 305) into the shrunk tube through the syringe. The concentration of Lumogen F Red 305 was 0.02 wt. % in this experiment. The resin was cured by
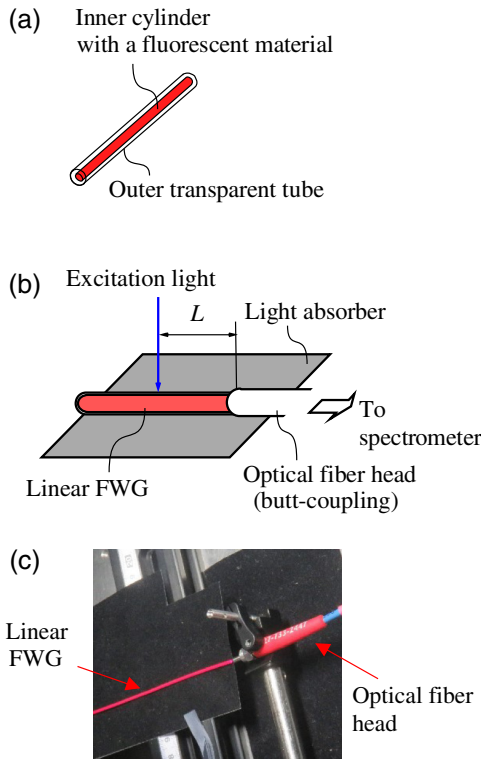
(a) Inner cylinder with a fluorescent material
Outer transparent tube

(b) Excitation light
L Light absorber
To spectrometer
Linear FWG
Optical fiber head (butt-coupling)

(c) Linear FWG
Optical fiber head

Fig. 4 Experimental setup and a photograph of 1-D position sensing. (a) The structure of a linear FWG.[18] (b) The linear FWG is butt-coupled to the optical fiber head and its single spot is irradiated. (c) A photograph of the linear FWG coupled to the optical fiber head.
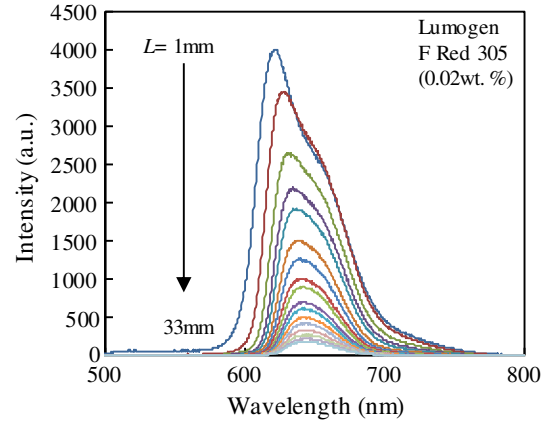
Fig. 5 Spectrum corresponding to each incident position of the excitation beam at 450 nm.

ultraviolet (UV) light irradiation. Finally, we cut the tube to detach the needle and filed the surface of the linear FWG with an abrasive paper.

As in the previous experiment, the following measurement was carried out in a darkroom. We recorded the redshift in the PL spectrum when we varied the distance L from 1 to 33 mm with a 2-mm step. The integration time of the spectrometer was set to 11 ms and data acquisition was repeated 20 times for averaging to suppress noise. As shown in Figs. 4(b) and 4(c), we excited a single point on the linear FWG by the laser emitting at 450 nm with its power of 348 μW.

The recorded spectra are shown in Fig. 5. We measured the spectrum for $L \leq 33$ mm beyond which the signal became so small. Compared to Fig. 2(a), the monotonic decrease of the intensity with the distance L is more gradual. This is expected from the geometrical confinement effect for the PL photons by the tubing configuration. The chromaticity coordinates calculated from these spectra are shown in Fig. 6(a). Here, we set the range of the distance L such that the change in the chromaticity coordinate y is monotonic. The coordinates calculated from the spectra measured at $L \geq 23$ mm have large uncertainties, indicating that the redshift is almost completed at $L = 23$ mm. By limiting the detection range to 3 mm $\leq L \leq 21$ mm, the distances L and y are well correlated, as shown in Fig. 6(b). Because the redshift in the spectrum, measured at $L = 1$ mm, is small, we also exclude the corresponding coordinate to improve the fitting. The fitting equation is given as

$$L = -3990348y^3 + 3607453y^2 - 1087247y + 109246,$$

$$3 \text{ mm} \leq L \leq 21 \text{ mm}. \tag{7}$$

Now, we have the calibration curve to determine the distance L from the measured spectrum. The detection range is 18 mm in this case.

Calculating the chromaticity coordinates is not the only means for determining L. For example, we define the following index I_2/I_1 based on the measured spectrum $S(\lambda)$

$$\frac{I_2}{I_1} = \frac{\int_{\Delta\lambda_{\text{NSA}}} S(\lambda)\text{d}\lambda}{\int_{\Delta\lambda_{\text{SA}}} S(\lambda)\text{d}\lambda}, \tag{8}$$
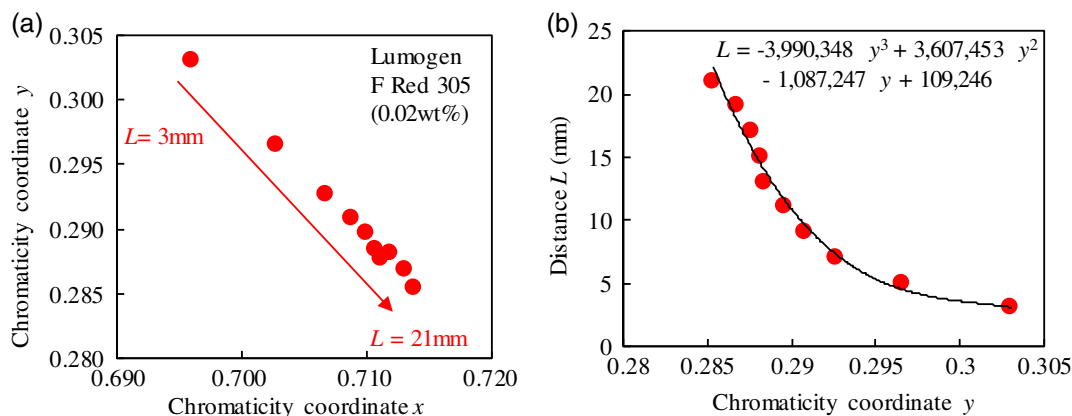
Fig. 6 Chromaticity coordinates calculated from the spectra in Fig. 5 and the CIE1931 color-matching functions. (a) The coordinates shift to a redder region as the distance L increases. (b) The distance L is well fitted by a cubic function of y.
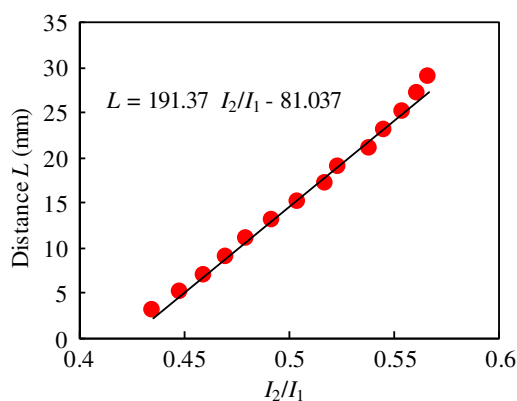

Fig. 7 The index I_2/I_1 calculated from the spectra in Fig. 5.

Fig. 8 A photograph of the experimental setup of PSD utilizing a scintillating fiber.

where $\Delta\lambda_{SA}$ and $\Delta\lambda_{NSA}$ are the wavelength range with and without self-absorption, respectively. Namely, I_1 represents the PL intensity over the wavelength range where self-absorption takes place, while I_2 is one over the range where no self-absorption takes place. We can set these ranges by examining the absorption and emission spectra of the luminescent materials. For example, these spectra for the organic dyes we used in our experiments are found in the literatures.[19,20]

Now, we try to relate I_2/I_1 to the distance L. Setting the integration range to 630 nm $< \lambda <$ 640 nm for $\Delta\lambda_{SA}$ and 650 nm $< \lambda <$ 655 nm for $\Delta\lambda_{NSA}$, we have calculated this index and the result is shown in Fig. 7. When we limit the range of L to 3 mm $\leq L \leq$ 29 mm, the distance is well fit by the following equation:

$$L = 191.37 \frac{I_2}{I_1} - 81.037, \quad 3 \text{ mm} \leq L \leq 29 \text{ mm}. \quad (9)$$

To summarize, we have determined the distance L based on the measured PL spectra by calculating two indices. The index I_2/I_1 gives a slightly wider detection range (26 mm) than the chromaticity coordinate y (18 mm) in this experiment.
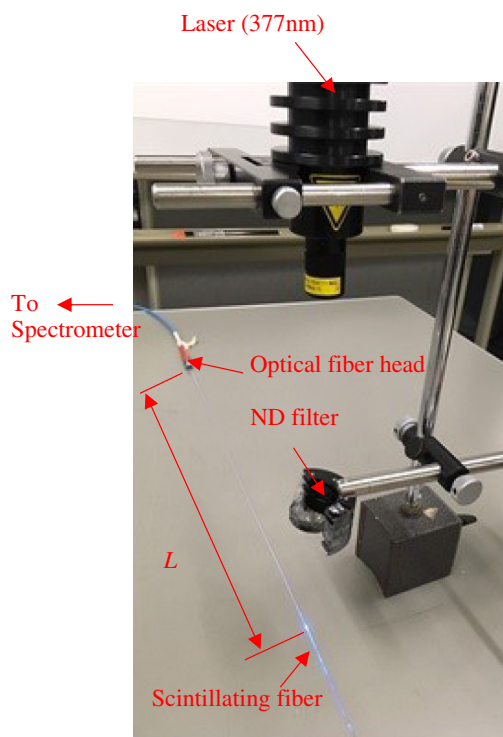
2.3 Extending the Detection Range

Our position-sensing technique relies on the spectral change. Once the redshift is completed, propagation over a further distance does not alter the shape of the PL spectrum. Hence, to extend the detection range further, we expect that the transmission loss within an FWG must be low. A commercial scintillating fiber has much lower transmission loss than our homemade linear FWG. As in the previous experiments, we have investigated the relation between the redshift of the PL spectrum and the distance L. The experimental setup is shown in Fig. 8. We used a scintillating fiber (Kuraray Co., Ltd., Japan, Model SCSF-78) for this experiment. Its length was 300 cm. A laser emitting at 377 nm was used as the excitation light source to excite the luminescent

material inside the fiber more efficiently. We varied the distance L from 10 to 290 cm with a 10-cm step. The power of the excitation light incident on the fiber through the neutral-density filter was measured to be 120.9 μW. The measurement was done in a darkroom.

As shown in Fig. 9, the intensity of the recorded spectra monotonically decreases as the distance L increases. Note that the range of L is much wider in this experiment.

In Fig. 10, we have plotted the distance L as a function of the chromaticity coordinate y calculated from the measured spectra. The distance L is well fit by the following equation:
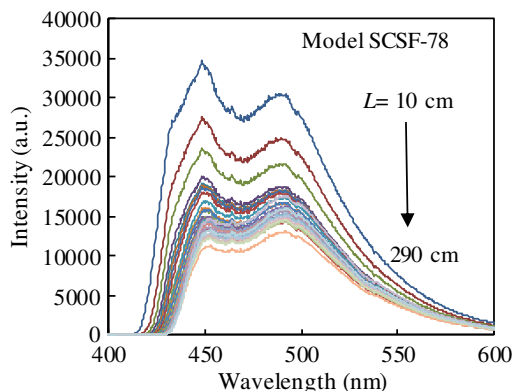

Fig. 9 Dependency of the spectrum on the distance L for the Kuraray scintillating fiber excited at 377 nm.
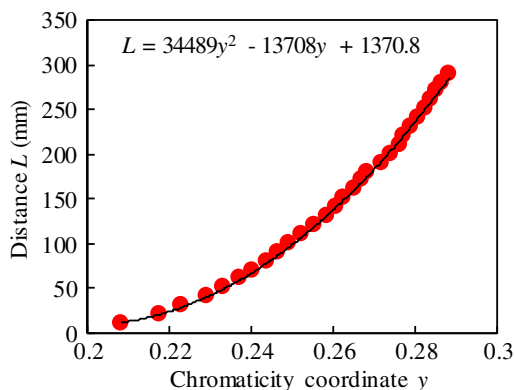

Fig. 10 The relation between the chromaticity coordinate y and the distance L.
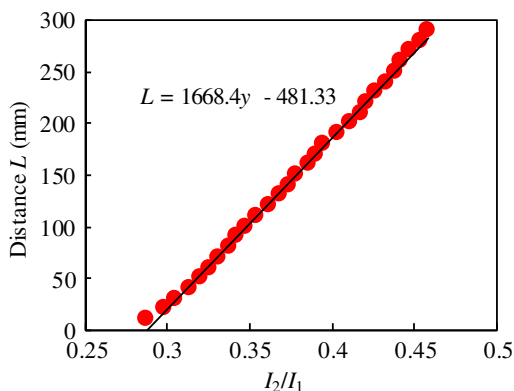

Fig. 11 The index I_2/I_1 calculated from the spectra in Fig. 9.

$$L = 34489y^2 - 13708y + 1370.8. \tag{10}$$

Again, we tried the index I_2/I_1 defined by Eq. (3) with the integration range of 440 nm $\leq \lambda \leq$ 455 nm for $\Delta\lambda_{SA}$ and 500 nm $\leq \lambda \leq$ 505 nm for $\Delta\lambda_{NSA}$. The result is shown in Fig. 11. The distance L is well fit by the following equation:

$$L = 1668\frac{I_2}{I_1} - 481.33. \tag{11}$$

The detection range is up to 280 cm for the two indices (y and I_2/I_1). Thus, using the commercial scintillating fiber with low-transmission loss in place of our homemade device, we extended the detection range by a factor of 100. In future, a custom-designed sensing medium would allow one to build a device suitable for a specific application.

2.4 Discussions

First, we discuss the signal-to-noise ratio of the PSDs based on this technique. Because the noise is essentially determined by the electronics involved, we focus on the signal size. There are two aspects here: the sensor-head design and the signal extraction process. The sensor-head design is specific to each application at hand. The PL spectrum at the end of a linear FWG is proportional to (a) the energy of the incoming radiation absorbed by the luminescent material, (b) its conversion efficiency to PL photons (quantum yield), and (c) the probability of the PL photons reaching the end of the linear FWG. These factors need to be considered specifically for each application. In addition, the signal extraction process plays an important role in determining the signal size. Calculating chromaticity coordinates is one option, which requires a spectrometer. It has a built-in slit, and the diffraction efficiency of its grating is limited. Hence, the PL photons are not efficiently utilized. In this regard, the index I_2/I_1 is preferred because we can measure this quantity directly. Namely, a photodiode covered by a bandpass filter would give I_1 and another photodiode with another bandpass filter would give I_2. A transistor connected to a photodiode enables the integration-mode operation, where the photo-generated charges are accumulated for a certain period of time. This is the building block of an image sensor.[21] If the radiation is incident at a constant rate, the signal size is proportional to this integration time. This condition applies for x-rays and also for decays of a radioactive material as long as its halftime is much longer than the integration time. In fact, low-intensity gamma-ray imaging was demonstrated with a long integration time.[22]

Second, we discuss the possibility of applying this sensing technique for radiation monitoring. When a 1-MeV gamma ray deposits its full energy in an evaporated CsI(Tl) layer, more than 25,000 electrons are generated in a crystalline Si photodiode coupled to it.[23] Photon yields of various scintillators are measured and expressed in units of photons/MeV.[24] The number for plastic scintillators is about 10,000 photons/MeV. Compton scattering is the dominant interaction for a matter with a low atomic number.[1] Let us start a rough calculation of signal size by assuming that a Compton event by a 1-MeV photon deposits 500 keV in a luminescent material. About 5000 photons are generated in the visible range. A photodiode would convert these photons to 2500 electrons if its quantum efficiency is 0.5.

A charge-sensitive amplifier is often used for radiation detection. Its equivalent noise charge is as small as 38 electrons.[25] Therefore, we expect that single photon counting of 1-MeV gamma rays is possible. If appropriate, we can resort to the integration-mode operation to increase the signal. One might wish to increase the detection efficiency by surrounding the sensing medium with a high atomic-number material such as lead glass tubing.[26] This would induce Compton scattering events more efficiently and the luminescent material would have a higher chance of interaction with the scattered x-rays. From these arguments, we expect that the basic concept described in Sec. 2.1 can be applied for radiation monitoring, although this needs to be confirmed by future experiments. In the experiments described in this paper, luminescent materials convert blue and UV photons from the lasers to PL photons. This phenomenon mimics the radioluminescence in a scintillator.

3 Two-Dimensional Position Sensing

In this section, we describe how the spectrum-based technique was applied for 2-D position sensing.[18]

3.1 Two-Stage Photoluminescence Conversion

As illustrated in Fig. 12(a), we configure a 2-D PSD by coupling two linear FWGs to the left and right edge surfaces of a planar FWG. The planer FWG contains a first fluorescent material. The linear FWG contains a second fluorescent material. We choose the fluorescent materials such that the PL photons of the first fluorescent material excite the second fluorescent material.

When an excitation beam hits a spot (X, Y) on the planar FWG, as depicted in Fig. 12(b), PL photons are generated and some of them enter the linear FWG at $x = L/2$ with a certain intensity distribution $I_{ex}(y)$. The PL photons also reach the linear FWG at $x = -L/2$ with a different distribution. A simple 2-D model can roughly reproduce these distributions as follows. Let us place an isotropic emitter at (X, Y) in a lossless medium and consider a photon propagating from this point to a narrow section at $(L/2, y)$. Denoting the width of this section as Δy, the probability of the photon reaching this section is equal to $\theta_d/2\pi$, where θ_d is the angle subtended by this section. Because the distribution $I_{ex}(y)$ is proportional to this probability, it is expressed as

$$I_{ex}(y) \propto \frac{\theta_d}{2\pi}$$
$$= \frac{1}{2\pi}\left\|\left|\tan^{-1}\frac{Y-y+\Delta y/2}{L/2-X}\right| - \left|\tan^{-1}\frac{Y-y-\Delta y/2}{L/2-X}\right|\right\|. \tag{12}$$

This equation generates a distribution that peaks at $y = Y$ and spreads out with increasing $L/2 - X$. If the medium is absorbing, the distribution would be narrower. We can extend this simple model to predict the performance of an energy-harvesting device such as an LSC.[27]

These PL photons from the planer FWG generate the second PL photons in the linear FWGs. Some of the second PL photons reach the end of the linear FWG and are guided to the spectrometer through the optical fiber. The spectra of the PL photons are recorded for each linear FWG: $S_R(\lambda)$ and $S_L(\lambda)$. To determine the incident spot (X, Y), we define the following two indices. As described in Sec. 2, quantification of the redshift in the PL spectra gives the coordinate Y. Here, we adopt the second index for determining the coordinate Y as follows:

$$L_Y = \frac{\int_{\Delta\lambda_{NSA}} S_R(\lambda)d\lambda}{\int_{\Delta\lambda_{SA}} S_R(\lambda)d\lambda}, \tag{13}$$

where the denominator of the index is the PL intensity over the wavelength range where self-absorption takes place, while the numerator is one over the range where no self-absorption takes place. Analogous to the charge division principle,[1–3] the coordinate X should be related to the ratio of $I_{ex}(y)$ at $x = \pm L/2$. Hence, we expect that L_X defined below is a measure of the coordinate X:

$$L_X = \frac{\int_{\Delta\lambda_{NSA}} S_R(\lambda)d\lambda}{\int_{\Delta\lambda_{NSA}} S_L(\lambda)d\lambda}. \tag{14}$$

Note that the spectra are integrated over the wavelength range where no self-absorption takes place in the second material. This excludes the effect of the coordinate Y in determining L_X.
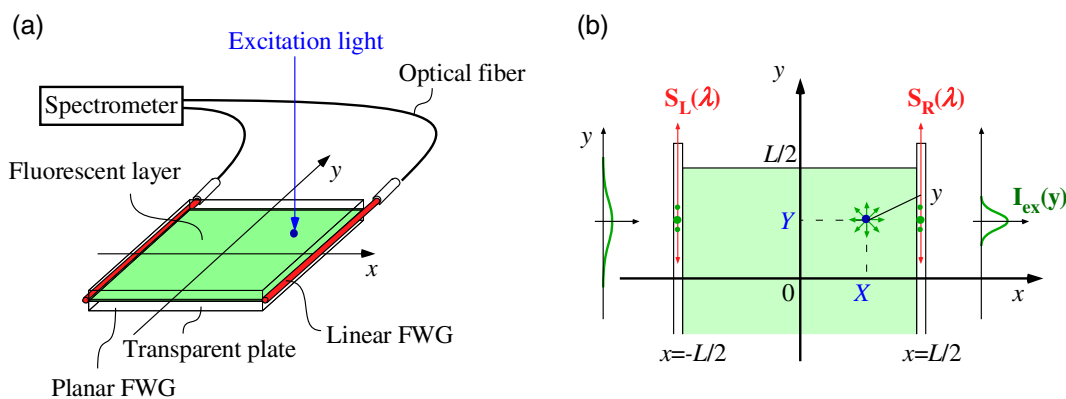

Fig. 12 Configuration of a 2-D PSD based on two-stage PL conversion with FWGs.[18] (a) A planar FWG and two linear FWGs constitute a sensor head. (b) The PL photons generated by the planar FWG enter the two linear FWGs with a certain intensity distribution, which can be roughly estimated by a simple geometrical calculation (see the text for detail).
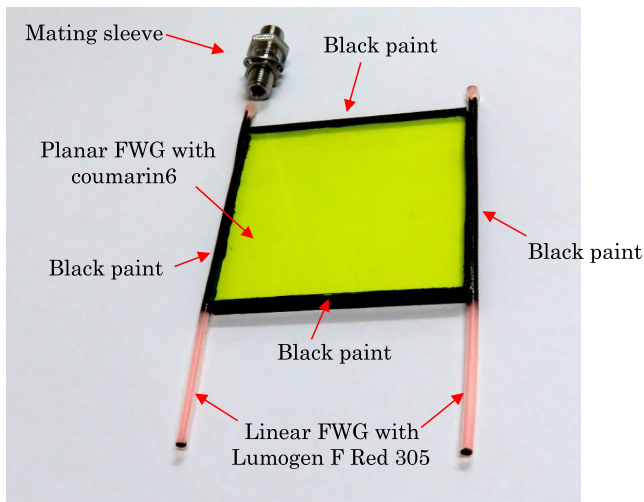
Fig. 13 Photograph of the sensor head.

3.2 *Experiment*

We fabricated a planar FWG with a mixture of Coumarin 6 (Sigma-Aldrich), UV-curable resin (NOA81) and two 50 mm × 50 mm × 4 mm acrylic plates, according to the method described in Ref. 17. Briefly, we sandwiched the mixture with two rectangular acrylic plates and cured the resin. The thickness of the phosphor layer was of the order of 0.1 mm. Linear FWGs were fabricated with a mixture of Lumogen F Red 305 and the same UV-curable resin by the method described in Sec. 2.2. Note that the PL photons from Coumarin 6 can excite Lumogen F Red 305.[19,20] The concentrations of Coumarin 6 and Lumogen F Red 305 were 0.07 and 0.01 wt. %, respectively. The length of the linear FWGs was about 90 mm. As shown in Fig. 13, the two linear FWGs were coupled to the two edge surfaces of the planar FWG with the UV-curable resin (NOA81). We painted the other two edge surfaces black to minimize light reflection there. The surfaces of the two linear FWGs were also painted black.

We used the same optical fibers (Ocean Optics, Model P400-21-VIS/NTR) for guiding the PL photons from each linear FWG to a spectrometer (Ocean Optics, USB2000). The end of each linear FWG was butt-coupled to each optical
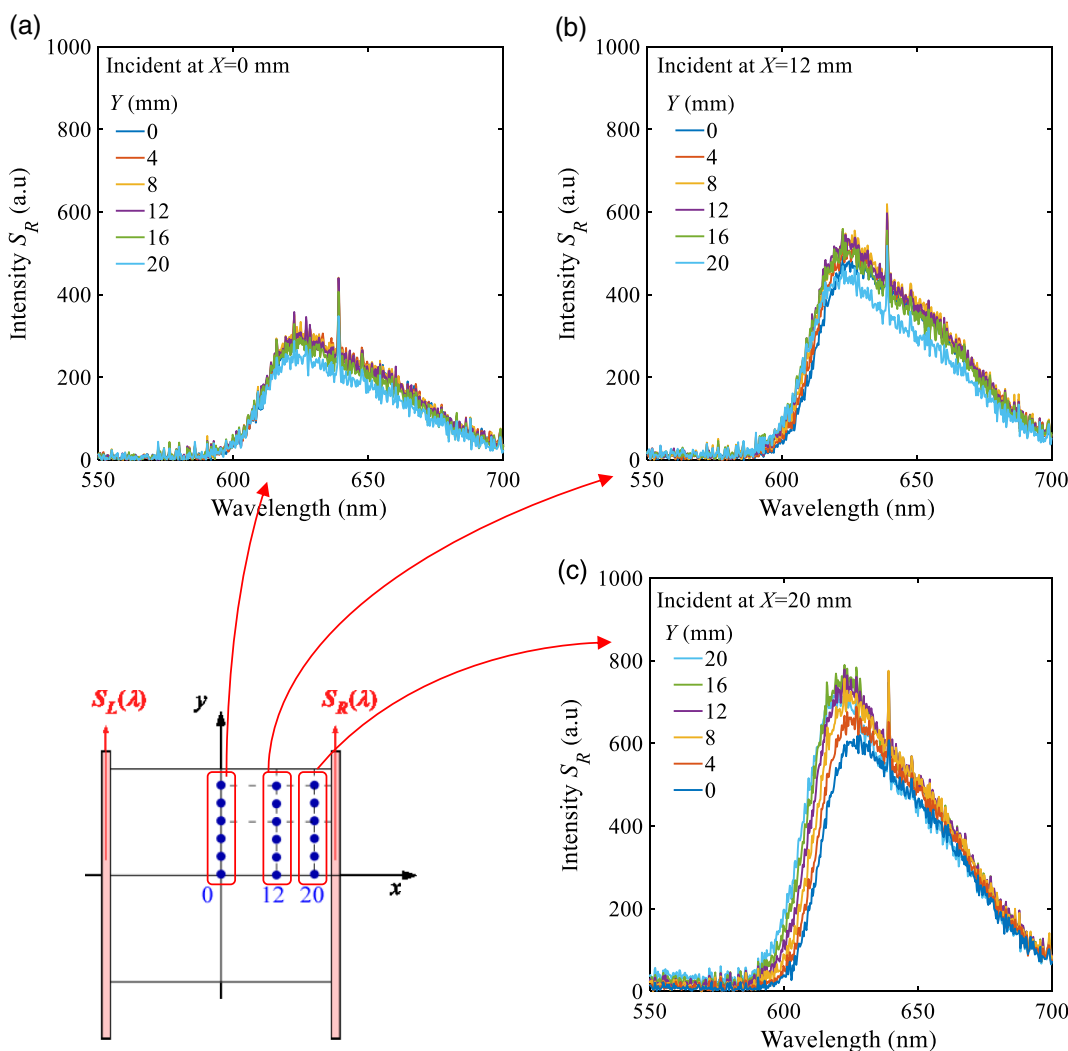

Fig. 14 The spectra of the PL photons from the right linear FWG. The excitation laser beam hits each point on the grid. In each plot, X is fixed and Y is varied.

fiber with a mating sleeve (Thorlabs, ADASMAV SMA to SMA mating sleeve). We placed the same laser unit (Z-Laser, ZZ30M18-F-450-pe) emitting at 450 nm with optical power of 3.4 μW on an $X - Y$ stage (Sigmakoki, TAM-1202SUU). The integration time of the spectrometer was set to 5 s. All the measurements were carried out in a darkroom.

We changed the excitation point (X, Y) in the first quadrant of the planar FWG, as shown in Fig. 12(b). The measured spectra are shown in Fig. 14. For each graph, the coordinate X is fixed, while the coordinate Y is varied. There are a couple of features to be noted here. First, as shown in Fig. 14(c), the intensity of the PL photons in the wavelength range from 600 to 640 nm decreases as Y increases. This redshift in the spectra becomes less evident at $X = 0$, as shown in Fig. 14(a). We attribute this observation to the fact that $I_{ex}(y)$ becomes wider and smaller at a small X. Second, the PL intensity at the wavelength >640 nm, where there is no self-absorption, decreases as Y increases. This trend is observed consistently, irrespective of X. Again, we believe that this is due to the function $I_{ex}(y)$: the number of the PL photons entering the linear FWGs decreases as Y increases.

3.3 Analysis

We calculated the index L_X using Eq. (14) and the measured spectra. As X increases, the index L_X increases monotonically, as shown in Fig. 15. It is strongly dependent on X, whereas its dependency on Y is relatively small. For example, we fit L_X as a function of X as follows:

$$L_X = Ae^{aX} = 1.28e^{0.0771X}. \tag{15}$$

The solid curve in Fig. 15 represents the fitting. The experimental data are more or less reproduced by this equation. Hence, we calculate the coordinate X from the index L_X as follows:

$$X = \frac{1}{a} \log \frac{L_X}{A} = \frac{1}{0.0771} \log \frac{L_X}{1.28}. \tag{16}$$

Because the index L_Y in Eq. (13) depends on the coordinate X via $S_R(\lambda)$, we calculated L_Y from each $S_R(\lambda)$ measured at
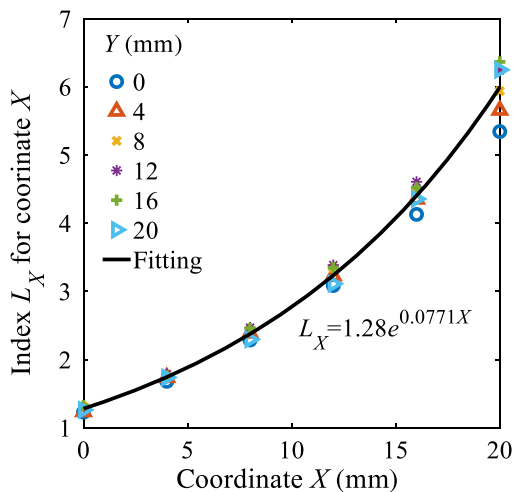
each X. As shown in Fig. 16, L_Y is nearly proportional to Y with the common intercept at $Y_0 = 4$ and different slope $\frac{dL_Y}{dY}$ for each X. Because the slope $\frac{dL_Y}{dY}$ depends on X, we need to relate $\frac{dL_Y}{dY}$ and X. As shown in Fig. 17, we found that $\frac{dL_Y}{dY}$ is more or less reproduced by a single exponential function as below:

$$\frac{dL_Y}{dY} = Be^{bX} = 0.0056e^{0.0661X}. \tag{17}$$

Denoting the average value of L_Y at $Y = 4$ as $L_{Y0}(= 1.18)$, the index L_Y is expressed as follows:

$$L_Y = Be^{bX}(Y - Y_0) + L_{Y0}$$
$$= 0.0056e^{0.0661X}(Y - 4) + 1.18. \tag{18}$$

Solving Eq. (18) for Y using Eq. (16), the coordinate Y is expressed as follows:

$$Y = \frac{L_Y - L_{Y0}}{Be^{bX}} + Y_0 = \frac{L_Y - 1.18}{0.0056e^{\frac{661}{771} \log \frac{L_X}{1.28}}} + 4. \tag{19}$$
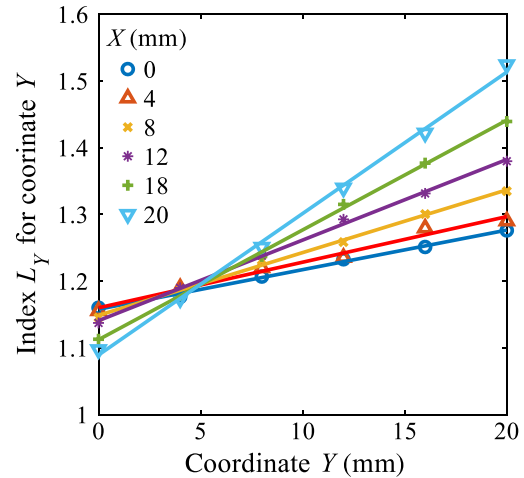

Fig. 16 Index L_Y calculated from Eq. (13). It is proportional to Y with the common intercept at $Y_0 = 4$ and different slope $\frac{dL_Y}{dY}$ for each X.
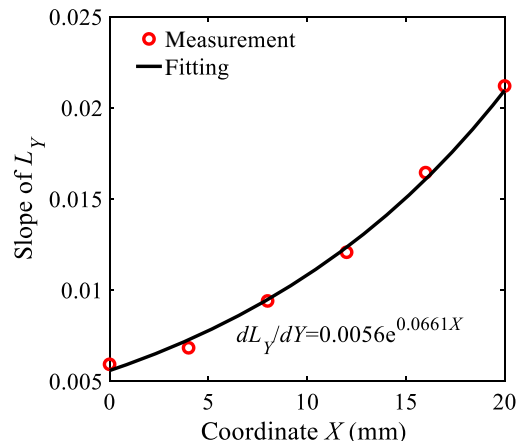

Fig. 15 The index L_X is regarded as a function of the coordinate X only.

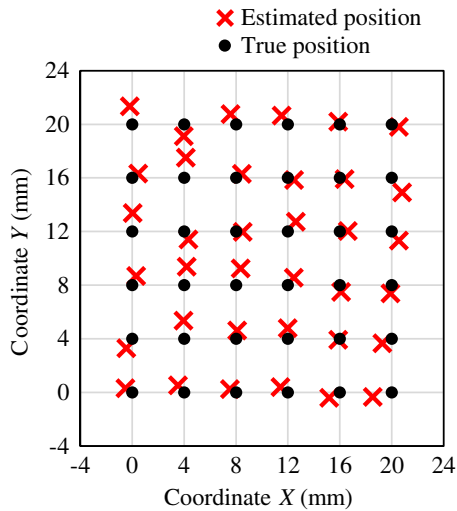**Fig. 17** Slope dL_Y/dY plotted as a function of the coordinate X.

Fig. 18 The true incident positions (dots) and the estimated ones (crosses).

Now, we have a set of expressions, Eqs. (16) and (19), which calculate (X, Y) from the measured PL spectra via indices L_X and L_Y.

3.4 Error

Using Eqs. (10) and (13), we estimated the incident position (X, Y). We compare the result with true positions in Fig. 18. The dots and crosses represent the true and the estimated positions, respectively. The discrepancy between them takes its maximum value of 1.5 mm for the incident position $(X, Y) = (0, 20)$.

4 Conclusion

We proposed a position-sensing mechanism based on redshift in PL spectrum. First, we demonstrated a 1-D PSD with a planar FWG. To confine the PL photons and increase the sensitivity, a linear FWG was fabricated by injecting a fluorescent material (Lumogen F Red 305) into a heat-shrink tubing. We investigated two indices to quantify the degree of redshift from the measured PL spectra. The first index was the CIE1931 chromaticity coordinates. The second index was the ratio of the PL spectra integrated over the wavelength ranges with and without self-absorption. The second index provided a slightly wider detection range (26 mm) than the first index (18 mm). We extended this range to 280 cm using a commercial scintillating fiber.

Second, we applied this concept to a 2-D PSD by utilizing two-stage PL conversion. Two linear FWGs were attached to the two opposing edges of a planar FWG. We chose the luminescent materials such that the PL photons generated in the planar FWG excited the material in the linear FWGs. Photon division in the planar FWG gave one coordinate of the incident point. The other coordinate was given by quantifying the redshift in the linear FWG. In experiment, we fabricated a 50 mm × 50 mm × 8 mm sensor head using a planar FWG with Coumarin 6 and two linear FWGs with Lumogen F Red 305. The maximum error for estimating the incident coordinates in the upper-right 20 mm × 20 mm region of the sensor head was 1.5 mm.

The conventional fiber sensors have high electromagnetic interference immunity, environmental durability, and a large sensing range. The technique investigated in this paper inherits these advantages. Unlike the conventional fiber sensors based on time of flight, signal is read out from one end of the fiber only. This enables insertion of the linear PSD into a narrow region. The two-stage PL conversion technique allows one to construct a 2-D PSD. The position-sensing technique proposed in this paper might be applicable for radiation monitoring, although this needs to be confirmed by future experiments.

References

1. G. F. Knoll, *Radiation Detection and Measurement*, 4th ed., pp. 47–51, 190–192, 361–362, 502–507, John Wiley & Sons, Inc., New Jersey (2010).
2. K. Desjardins, C. Menneglier, and M. Pomorski, "Single crystal CVD diamond membranes as position sensitive x-ray detector," *J. Instrum.* **12**, C12046 (2017).
3. W. Wang et al., "High-performance position-sensitive detector based on graphene-silicon heterojunction," *Optica* **5**(1), 27–31 (2018).
4. D. Qian, W. Wang, and I. J. Busch-Vishniac, "A method for measurement of multiple light spot positions on one position-sensitive detector (PSD)," *IEEE Trans. Instrum. Meas.* **42**(1), 14–18 (1993).
5. C. T. Chiang and Y. T. Hou, "A CMOS monolithic calibrated position-sensitive detector (PSD) for detecting light-spot position applications," in *Proc. IEEE Int. Conf. Mech. and Autom.*, pp. 862–867 (2016).
6. R. Porrazzo et al., "Self-balancing position-sensitive detector (SBPSD)," *Sensors* **15**(7), 17483–17494 (2015).
7. M. Javadi et al., "Hybrid organic/inorganic position-sensitive detectors based on PEDOT-PSS/n-Si," *Appl. Phys. Lett.* **112**, 113302 (2018).
8. I. Fujieda et al., "Radiation imaging with 2D a-Si sensor arrays," *IEEE Trans. Nucl. Sci.* **39**, 1056–1062 (1992).
9. K. T. V. Grattanand and T. Sun, "Fiber optic sensor technology: an overview," *Sens Actuators A Phys.* **82**, 40–61 (2000).
10. D. L. Chichester, S. M. Watson, and J. T. Johnson, "Comparison of BCF-10, BCF-12, and BCF-20 scintillating fibers for use in a 1-dimensional linear sensor," *IEEE Trans. Nucl. Sci.* **60**(5), 4015–4021 (2013).
11. I. Toccafondo et al., "Distributed optical fiber radiation sensing in a mixed-field radiation environment at CERN," *J. Lightwave Technol.* **35**(16), 3303–3310 (2017).
12. I. Parola et al., "High performance fluorescent fiber solar concentrators employing double-doped polymer optical fibers," *Sol. Energy Mater. Sol. Cells* **178**, 20–28 (2018).
13. M. Ohta et al., "A position sensitive detector based on red-shift in photoluminescence spectra," *Proc. SPIE* **10768**, 107680N (2018).
14. J. S. Batchelder, A. H. Zewail, and T. Cole, "Luminescent solar concentrators. 1: theory of operation and techniques for performance evaluation," *Appl. Opt.* **18**(18), 3090–3110 (1979).
15. J. S. Batchelder, A. H. Zewail, and T. Cole, "Luminescent solar concentrators. 2: experimental and theoretical analysis of their possible efficiencies," *Appl. Opt.* **20**(21), 3733–3754 (1981).
16. R. W. Olson, R. F. Loring, and M. D. Fayer, "Luminescent solar concentrators and the reabsorption problem," *Appl. Opt.* **20**(17), 2934–2940 (1981).
17. I. Fujieda and M. Ohta, "Angle-resolved photoluminescence spectrum of a uniform phosphor layer," *AIP Adv.* **7**, 105223 (2017).
18. Y. Tsutsumi et al., "Two-stage photoluminescence conversion for two-dimensional position sensing," *Proc. SPIE* **10768**, 107680O (2018).
19. E. F. Schubert, *Light Emitting Diodes*, 2nd ed., p. 350, Cambridge University Press, New York (2006).
20. O. M. Ten Kate, K. M. Hooning, and E. van der Kolk, "Quantifying self-absorption losses in luminescent solar concentrators," *Appl. Opt.* **53**(23), 5238–5245 (2014).
21. G. P. Weckler, "Operation of p-n junction photodetectors in a photon flux integrating mode," *IEEE J. Solid-State Circuits* **2**(3), 65–73 (1967).
22. I. Fujieda et al., "Two operation modes of 2D a-Si sensor arrays for radiation imaging," *J. Non-Crystalline Solids* **137**–**138**, 1321–1324 (1991).
23. I. Fujieda et al., "X-ray and charged particle detection with CsI(Tl) layer coupled to a-Si:H photodiode layers," *IEEE Trans. Nucl. Sci.* **38**(2), 255–262 (1991).
24. I. Holl, E. Lorenz, and G. Mageras, "A measurement of the light yield of common inorganic scintillators," *IEEE Trans. Nucl. Sci.* **35**(1), 105–109 (1988).

25. M. Beikahmadi and S. Mirabbasi, "A low-power low-noise CMOS charge-sensitive amplifier for capacitive detectors," in *IEEE 9th Int. New Circuits and Syst. Conf.*, pp. 450–453 (2011).
26. I. Fujieda et al., "Electron transmission and avalanche gain in narrow lead glass tubing," *IEEE Trans. Nucl. Sci.* **32**(1), 687–691 (1985).
27. I. Fujieda et al., "Simple analytical model for optical efficiency of an energy-harvesting projector," *Proc. SPIE* (2019).

Yasuhiro Tsutsumi is an assistant professor at Ritsumeikan University. He received BE, ME, and PhD degrees from Osaka Prefecture University in 2007, 2009, and 2012, respectively. His current research interests include optical sensing, optical fiber devices, and optical communications. He is a member of SPIE, OSA, IEEJ, IEICE, and JSAP.

Ryo Matsumura has been working on this position-sensing technique since December 2017. He started his graduate studies, in April 2019, at Ritsumeikan University.

Masamichi Ohta worked on display-integrated photovoltaic systems and this sensing technique. He received his ME degree from Ritsumeikan University in March 2019. He is now with Hoshiden Corp., Japan.

Ichiro Fujieda received his PhD from the University of California, Berkeley, in 1990. He was with Xerox Palo Alto Research Center from 1990 to 1992 and NEC Corporation from 1992 to 2003 before joining Ritsumeikan University in 2003.